

RESEARCH ARTICLE

A NOVEL MODEL FOR DETECTING LUNGS TUMOUR AND ABNORMAL LYMPH NODES IN PET-CT IMAGES

¹S.Meenakshi Sundaram,²U.Revathy,³S.Pradeep

¹*Associate Professor - Department of Computer Science and Engineering, Aringer Anna College of Engineering and Technology, Dindigul, India, E-mail bosemeena@gmail.com*

²*Assistant professor- Department of Computer Science, Government Arts College for women, Sivagangai, India, E-mail urevathymeena@gmail.com*

³*Assistant professor- Department of Computer Science, Pannai College of Engineering and Technology, Sivagangai, India, E-mail csspradeep@gmail.com*

ABSTRACT

Article History:

Received 22th Nov 2016

Received in revised form 28th Nov 2016

Accepted 28.11.2016

Published on 30.12.2016

Index Terms—Abnormal lymph node detection, discriminative method, lung tumor, multistage modeling, spatial features.

Corresponding author:

S. Pradeep

Email: csspradeep@gmail.com

Analysis of primary lung tumors and disease in regional lymph nodes is important for lung cancer staging, and an automated system that can detect both types of abnormalities will be helpful for clinical routine. In this paper, we present a new method to automatically detect both tumors and abnormal lymph nodes simultaneously from positron emission tomography—computed tomography thoracic images. We perform the detection in a multistage approach, by first detecting all potential abnormalities, then differentiate between tumors and lymph nodes, and finally refine the detected tumors for false positive reduction. Each stage is designed with a discriminative model based on support vector machines and conditional random fields, exploiting intensity, spatial and contextual features. The method is designed to handle a wide and complex variety of abnormal patterns found in clinical datasets, consisting of different spatial contexts of tumors and abnormal lymph nodes. We evaluated the proposed method thoroughly on clinical datasets, and encouraging results were obtained. The watershed transforms combines aspects of both region-based and edge-based approaches to image segmentation. The regions are built by pixel grouping (region-based), whereas the edges of the regions are located based on image discontinuities (edge-based). This section presents the basic algorithm as well as more efficient algorithms for its implementation.

I. INTRODUCTION

LUNG cancer is the most common cause of cancer-related death in men and women, and is responsible for

1.3 million deaths annually, as of 2008 [1]. In particular, non small cell lung cancer (NSCLC) is the most prevalent type of lung cancer, accounting for about 80%

of all cases [2]. Staging, which assesses the degree of spread of the cancer from its original source, is the most important factor affecting the prognosis and potential treatment of lung cancer. For NSCLC, the tumor node metastasis (TNM) staging is the internationally agreed system, which involves analysis of the primary lung tumor, regional lymph nodes and distant metastases [2]. The the primary lung tumor and the locations of the abnormal regional lymph nodes indicate a stage IA to IIIB NSCLC, while any distant metastases suggest a stage IV NSCLC. Positron emission tomography—computed tomography (PET-CT) with *F-fluoro-deoxy-glucose* (FDG) tracer is now accepted as the best imaging technique for non-invasive staging [3]. While the CT scan provides anatomical information, it has relatively low soft tissue contrast causing difficulties in separating abnormalities from the surrounding tissues. On the other hand, the PET scan has high contrast and reveals increased metabolism in structures with rapidly growing cancer cells, but their localization is limited by the low spatial resolution in PET images. The integrated PET and CT scan thus provides complementary pathological and anatomical information. In current clinical routine, the localization and characterization of abnormalities need to be performed manually by examining all PET-CT slice pairs. To assist this time-consuming process and potentially provide a second opinion to the reading physicians, an automated system that can provide fast and robust detection is highly desirable. In this work, our objective is to design a fully automatic methodology for simultaneous detection of primary lung tumors and disease in regional lymph nodes from PET-CT thoracic images. The problem exhibits two main challenges. First, although PET indicates areas with high uptake activities, it can also highlight non pathological areas (e.g., in myocardium), and the standard uptake value (SUV), which is a semi-quantitative measure of normalized radioactivity concentration, normally exhibits high inter-patient variances. Second, separations between lung tumors and abnormal lymph nodes are difficult. Although they may be differentiated by segmenting the lung fields from CT images, if tumors extent to the surrounding organs especially the mediastinum, such segmentations may not be reliable. For complex cases involving tumors invasion into the mediastinum or lymph nodes abutting the lung field, the ability to differentiate between the two types of abnormalities are more challenging. In our

prior work [4], we proposed a discriminative model with local-, spatial-, and object-level features for detecting tumor and abnormal lymph nodes. Whereas good detection performance was observed, several issues should be addressed:

- 1) the method required the surrounding regions of tumors and abnormal lymph nodes to be accurately classified, which involved a heuristic-based grouping operation to separate the surrounding regions from the mediastinum,
- 2) the regions belonging to a tumor or lymph node volume were classified individually, which could result in inconsistent labeling of the set of regions within a 3-D volume, and 3) the high-uptake Myocardium introduced false positives in the detection results. Therefore, we now propose a new method, and the main distinctive characteristics of our method are: 1) a multistage detection is designed, where stage-1 detects all abnormalities from a 3-D image set, stage-2 differentiates the detected abnormalities into tumors and abnormal lymph nodes, and stage-3 reduces the false positives of tumors; 2) each stage is optimized with a structural

Discriminative approach, specifically we choose to employ support vector machine (SVM) [5] for classifying individual regions due to its high performance in classification without a generative Model, and the conditional random field (CRF) [6] for its capability in exploring the contextual information between multiple regions for a simultaneous classification of all regions in a 3-D volume; and 3) a number of new feature sets are designed, including various types of intensity, spatial and contextual features, for each stage of the detection method. We test our method on clinical PET-CT image sets, where multiple tumors and abnormal lymph nodes may co-exist and introduce extra complexities. For example, the multiple abnormalities may exhibit large differences in uptake activities; and lymph nodes may reside very closely to the lung tumor and become particularly difficult to separate. The datasets also show a wide variety of abnormal patterns, with tumors of various shapes and spatial extents, and lymph nodes of different sizes and locations.

A. Related Work

Up to now, the amount of publications on simultaneous detection of lung tumors and disease in regional lymph nodes is limited. In our recent work [7], a region-based

approach with spatial information was reported, which however, proposed a detection method mainly to facilitate image retrievals, rather than focusing on optimization of the detection performance. Furthermore, the method required a separate class of tumor border, to work around the issue that the surrounding areas of tumors were often confused with the mediastinum. Such a tumor-border class complicated the training process, which was quite unnatural for the clinical process. Our later work [4] avoided such an issue with a multilevel discriminative model and more comprehensive spatial features, but also posed several improvement opportunities, which we explained in the previous section. A similar type of work is on lung tumor detection, which first detects all abnormalities, then extracts only those that are highly representative of lung tumors. By first segmenting the lung field, a threshold and fuzzy-logic based approach is then used to detect the lung tumors [8], but the detection performance is quite sensitive to the delineation accuracy of the lung field. Another approach attempts to handle tumors lying close to the edge of lung fields by incorporating the location, intensity, and shape information [9], but the method could potentially result in a large number of false positives with the predefined SUV thresholds. To reduce the false positives detected in the mediastinum, learning-based techniques with tumor-specific features were proposed [10], [11], but the methods were based on empirical studies of SUV distributions and tumor sizes, and did not seem to consider abnormal lymph nodes in the thorax. Another category of abnormality detection is to detect all instances from PET images, regardless of their types. Such approaches include a texture-based classification method [12], a water-shed based algorithm integrated with morphological measures [13], and a region-based SUV threshold computed based on the object and background ratio [14]. While the former two techniques operate on user-selected volume-of-interest (VOI) or potential lesions, the last one assumes a large portion of the mediastinum to be normal. It was also shown that the detected abnormalities could be used to infer the cancerous status of a patient [15], which however, did not assess the detection performance of tumors or lymph nodes. There are also a number of existing works on lymph node detection, mostly on CT images. Most of these methods utilize the segmentation of the anatomical structures in mediastinum, such as airways, aorta and pulmonary

artery [16]–[19]. A Hessian matrix for detecting the blob-like shaped lymph nodes is also used [18], [20]. A deformable registration approach has been recently proposed to restrict the search area of the blob detectors [20], using a probabilistic mediastina lymph node atlas created by combining all database images with manually delineated lymph nodes. A different discriminative method was also proposed to detect lymph nodes based on comprehensive appearance and spatial features [19]. Detection methods for other types of lymph nodes include the directional difference filtering for abdominal nodes [21] and the marginal space learning for axillaries nodes [22]. The detection performances of these approaches are usually highly related to the segmentation accuracy of anatomical structures, which is however, hard to avoid for CT images. These approaches also focus on the lymph nodes only, not considering cases with tumors, especially if they affect the appearances of the anatomical structures in the mediastinum. Another often studied area for lung tumor and regional lymph nodes is segmentation, including a number of different methods for tumor volume delineation on PET images with a comprehensive review in [23], those for CT [24]–[26], and PET-CT images [27]–[29], and lymph node segmentations on CT images [30]–[32]. While segmentation techniques normally assume a prior knowledge of presence of abnormalities with user annotated initial seeds or bounding boxes, detection algorithms aim to determine such presences and focus on optimizing the detection recall and precision.

B. Outline

The paper is structured as follows. Section II gives an overview of our proposed method. Sections III, IV and V describe the three stages of detection—abnormality detection, tumor and lymph node differentiation and tumor region refinement. Section VI introduces the materials and evaluation methods. The experimental results and discusses are presented in Sections VII and VIII concludes the paper.

II. SUMMARY OF OUR PROPOSED METHOD

An intuitive idea of detecting tumors and abnormal lymph nodes in a discriminative construct is to assign one most probable label to each voxel. Specifically, let be the 3-D image set of a thoracic scan with voxels.

Define the set of labels ,lung field, mediastinum, tumor and abnormal lymph nodes, and a label set with one label for each voxel . Then, the solution is to compute the maximum *a posteriori* estimates using various types of classifiers(1) However, it is difficult to design a set of features sufficient for discriminating the four voxel classes in a single classification step. For example, the main distinctive feature between and is the spatial context, i.e., being within the lung field or mediastinum; But how to describe this spatial feature without first labeling the regions of and is a challenge. Furthermore, in complex cases where the tumors are adjacent to or invading into the mediastinum, the surrounding areas of tumors might be classified as mediastinum, hence causing more difficulties in differentiating from . We thus propose a multistage discriminative model to detect tumors and abnormal lymph nodes. First, we made no distinction between the two types, and classified the voxels into the lung field (), mediastinum (), and abnormal region of interest (ROI), with two levels of features and SVM-based soft labeling. Next, we designed a CRF model with unary and pairwise features in 3-D space to differentiate the detected abnormal volumes into tumors () and abnormal lymph nodes (). Last, we formulated another 3-D CRF model to refine the detected tumors for false positive reductions.

III. MATERIALS AND EVALUATION METHODS

Our dataset used in this study consists of image scans from 85 patients diagnosed with NSCLC, acquired using a Siemens TrueV 64 PET-CT scanner at the Royal Prince Alfred Hospital, Sydney. By selecting image slices covering all abnormalities in the thorax from each patient scan, the dataset contained 85 3-D image sets comprising 2480 transaxial PET-CT slice pairs. The reconstructed matrix size of each transaxial CT slice was 512x 512 voxels with a slice thickness of 3 mm. For PET images, the matrix size was 168 168 with a slice thickness of 5 mm. During the preprocessing, the PET images were linearly interpolated to the same voxel size as the CT images, and FDG uptake normalized into SUV based on the injected dose and patient's weight. We will simply refer to a slice pair as a slice in the following. For each 3-D image set, a senior expert indicated the quantities of lung tumors and abnormal lymph nodes, with descriptions of their locations and

characteristics. This senior expert has read over 8000 PET-CT lung cancer studies.

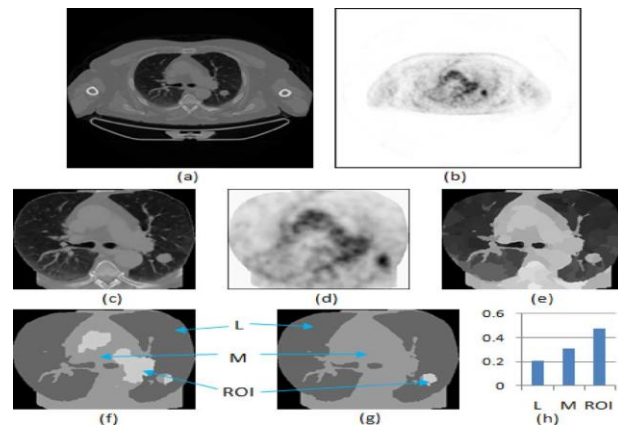


Fig. 1. Illustration of stage-1 on abnormality detection. (a) A trans axial CT slice. (b) The co-registered PET slice. (c) The CT slice after preprocessing. (d) The PET slice after preprocessing. (e) The regions created using quick-shift clustering. (f) The detection output based on low-level features, with blue arrows indicating the correspondence between gray scale values and region types. (g) The second detection output based on high-level features. (h) The soft labeling vector of the detected ROI region.

To encode these ground truths for training and testing, we also created the following for each tumor and abnormal lymph node: 1) an approximate 3-D bounding box indicating its span of, and coordinates; and 2) a key slice showing its most prominent feature (e.g., size and spatial extent) with a corresponding mask depicting the region labeling. A total of 93 lung tumors and 65 abnormal lymph nodes were annotated, and grouped into several categories, as shown in Table I. Linear-kernel SVMs was used as the classifiers in this work. Based on our experiments, the linear-kernel construct was more suitable than the polynomial and Gaussian radial basis functions. The training was performed by first selecting 10 3-D image sets as the training pool, which roughly comprised of two annotated volumes for each category of tumors and abnormal lymph nodes. From this training pool, an initial set of training samples was chosen manually to represent the typical patterns of different classes. A bootstrapping approach was then conducted to include

training samples incrementally until no further improvements could be observed based on the training pool. No training samples were replaced and only additional samples were added during this bootstrapping procedure. The training pool was limited to 10 3-D image sets to minimize the risk of over-fitting; note that since 10 3-D sets actually contained a large number of image regions that could be used as training samples, the bootstrapping procedure was effective in reducing the size of training samples to about only 10% from the training pool. We evaluated the recall, precision, and F-score

of the detection results at each stage (22),(23),(24) where TP, FN, and FP were the numbers of true positive, false negative and false positive detections, which were all object (i.e., volume) based. In the PASCAL standard [41], an object detected with at least 50% overlap with the ground truth volume would be considered TP. Since in our dataset the ground truth volume was an approximate 3-D bounding box, TP was determined based on visual inspections of all slices, with the criteria that 1) The detected volume depicted the actual abnormality relatively closely, with imprecise delineations allowed around the boundaries; and 2) a volume was labeled (or) consistently throughout the stack of slices, without any mislabeling within the detected volume. Inclusion of the latter criterion implied a more stringent requirement than the PASCAL standard. In addition, the detection performance was also measured with receiver operating characteristics

(ROC) curves. The ROC curve was a plot of true positive rates (TPR) versus false positive rates (FPR), by varying the classification thresholds based on the probability estimates of the labeling outputs. The probability estimates of all regions from a volume were averaged as the object-level measure, which was gathered for all TP, FN, and FP volumes. The area under the curve

(AUC) was then computed to quantify the detection performance. Furthermore, the discriminative power of each type of feature was evaluated by analyzing the probability estimates of different classes. For features with low dimensions, the separation of feature spaces was visualized based on the data distribution of our dataset.

IV.EXISTING METHOD

A. Detection of Abnormalities

We first report the recall, precision and F-score of abnormality detections on our dataset. A 3-D ROI volume (regardless of tumor or abnormal lymph node) that was successfully detected was considered as true positive. A missed detection was false negative. A detected ROI volume that was actually a normal thoracic area was then false positive. The constant in (3) was determined as 0.18 using the learning-based procedure. As shown in Table I, with low-level features only, our method achieved 99.4% recall of abnormalities, with only one false negative detection, but at the expense of 51 false positives.

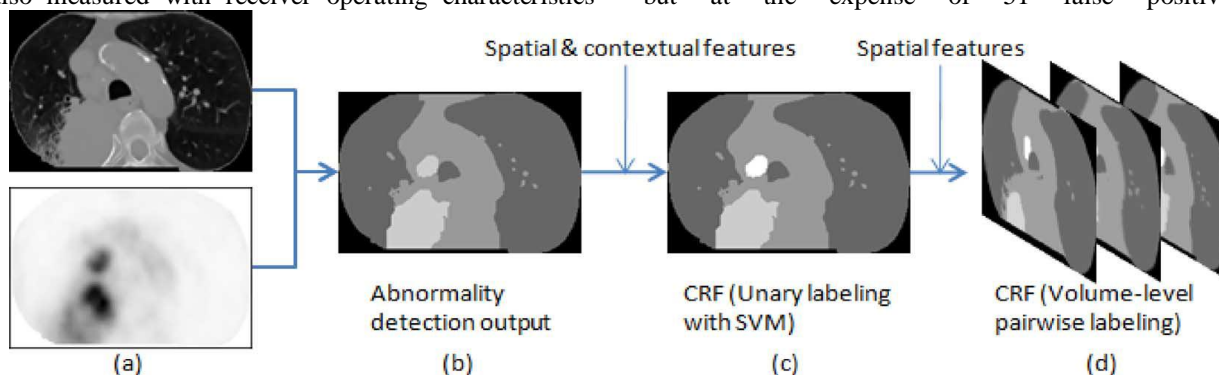


Fig. 2. Illustration of stage-2 on tumor and lymph node differentiation. (a) Transaxial PET-CT slice. (b) Abnormality detection output—two ROIs detected. (c) Region-level labeling with the unary term based on spatial and contextual features—the two ROIs labeled as one tumor (gray) and one abnormal lymph node (white). (d) Volume-level labeling with the pairwise term based on 3-D spatial features.

	LOW	HIGH		LOW	HIGH
TP	157	155	Recall	99.4	98.1
FN	1	3	Precision	75.5	88.6
FP	51	20	F-Score	85.9	93.1

With the inclusion of high-level features, the false positives were largely reduced and the precision of detection increased by about 13%. Although two more false negatives were produced with the high-level features, the overall performance was higher (93.1% F-score) with a better balance between the recall and precision. The false negatives were all at abnormal lymph nodes, which were hard to detect due to their relatively low SUVs close to

TABLE II
RESULTS OF ABNORMALITY DETECTION
WITH LOW-LEVEL FEATURES ONLY OR
INCLUDING THE HIGH-LEVEL FEATURES.
(A) NUMBERS OF TRUE POSITIVES (TP),
FALSE NEGATIVES (FN), AND FALSE
POSITIVES (FP). (B) RECALL, PRECISION,
AND F-SCORE (%)

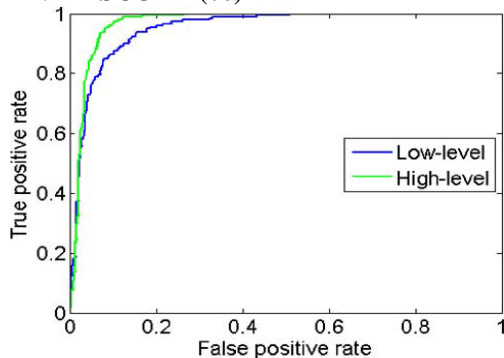


Fig.3. ROC curves of abnormality detection, for low-level features only or including the high-level features.

the mediastinum. The false positives were detected at the high uptake regions in the mediastinum, because of either reasons: 1) the region represented high-uptake myocardium; or 2) the tumor in the same image set exhibited quite low SUV and hence the high-uptake region showed similar SUV to the tumor. For case 1), the stage-3 of our method targeted the detection of high uptake myocardium, and the results will be

presented in the later section. For case 2), since the high-level feature worked based on the SUV contrast between ROIs and the mediastinum, if the contrast level was really low, such false positives could then remain. high-level features. The AUC values of both curves were 0.9512 and 0.9691, respectively. Although the difference in AUC was small, it can be seen from the curves that at near 100% true positive rates, there was large reduction in false positive rates with the high-level features. The discriminative power of the low-level intensity features can be seen from Fig.4, showing a clearer separation between the three types of structures with the normalized SUV than the original SUV. We also evaluated the feature space based on the third quartile of SUV for and and the first quartile for ROI to measure the overlaps between the upper SUV range of and the lower SUV range of ROI; and a similar difference in the feature separation was observed. Fig.5 shows the feature space of a subset of the high-level features: ratio of average SUV between ROI region and the mediastinum, —ratio between and the lung field, and average SUV of . The feature space was computed for both the real ROIs and the false positives detected with the low-level features. The two clusters were well separated for each feature dimension, but quite close at the separation boundary and hence the remaining false positive or negative

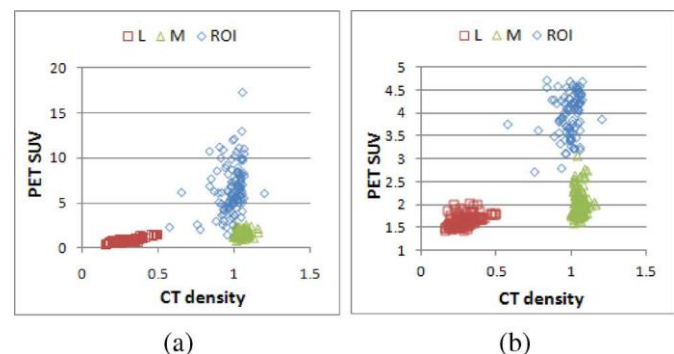


Fig.4. Scatter plots for the lung field, mediastinum and ROI areas based on (a) the original SUV and (b) the normalized SUV.

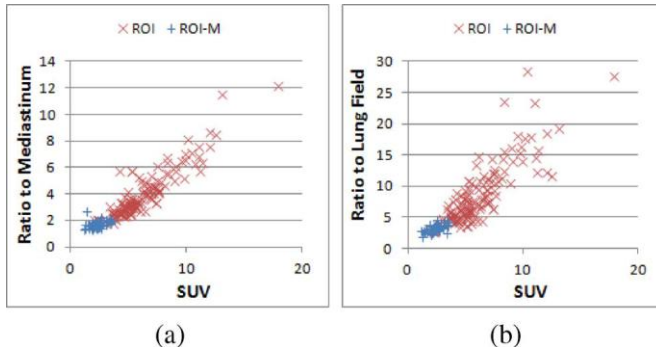


Fig.5. Scatter plots of for ROI (the real ROI regions) and ROI-M (the regions initially detected as ROIs at low-level), showing the SUV ratios between the detected ROI and (a) the mediastinum and (b) the lung field.

ROIs after the labeling with high-level features. The discriminative power was enhanced when all four feature dimensions were integrated with different feature weights.

B. Computational Efficiency

Table X shows the average computational time for a 3-D image set (about 30 transaxial slice pairs). Our method was implemented in Matlab v2009b, running on a standard PC with a 2.66-GHz dual core CPU. In total, an average of 89.8 s was required, with about 41% of the time spent on region clustering.

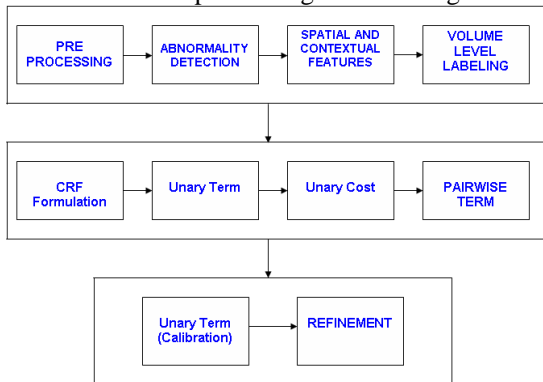


Fig 6. Block Diagram of Existing Method

The extraction of unary features for stage-2 was the second most time consuming component taking 21.9 s. The low-level labeling at stage-1 took about 12.5 s, which was mainly incurred by the SUV normalization step.

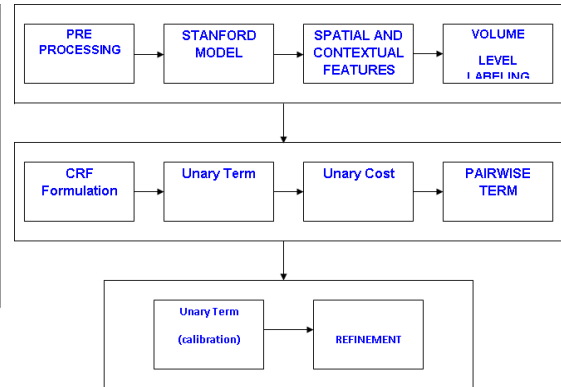


Fig 7. Modified Block Diagram of Proposed System

The other processing was much faster with lower feature dimensions. The following Fault identified and discussed in the Existing system Region based approach with spatial information method Learning based techniques with tumor specific features multistage discriminative model (MSD model).

WATERSHED ALGORITHM

The image to which the watershed is applied should have each region of the partition to be computed marked by a gray-scale minimum, and the boundaries of the regions marked by gray-scale maxima. As the image to be segmented usually does not satisfy these requirements, it is preprocessed to produce an image that better satisfies them. Three approaches are used to reduce over segmentation, the first part of all three paths is preprocessing and filtering, in which the aim of this step is to reduce the number of local minima and enhance the object boundaries. The result of this step is referred to as the segmentation image. The watershed can optionally be applied directly to this image. The aim of the filtering and preprocessing step is to create a segmentation image that satisfies the requirements for good watershed segmentation. This step has been divided into a filtering part, which has the aim of filtering noise and hence reducing the number of spurious local minima, and a preprocessing part, which aims to enhance the region boundaries.

Watershed with Markers

The watershed with markers can also be visualized by using the immersion simulation. The difference is that instead of punching holes at each local minimum of the topographic surface, holes are only punched at

positions specified by a set of markers. As only one region is created per marker, having fewer markers will reduce the number of regions in the final segmentation. To use markers in practice, one creates a marker image, which is a binary image in which each connected component corresponds to a marker, or, using the immersion visualization, a “hole” through which water will flow. A marker can range in size from a single pixel to a large, connected component. These markers are imposed on the image on which the watershed is to be calculated through minima imposition or swamping.

V. CONCLUSION AND FUTURE WORK

We have presented a fully automatic detection method for lung tumor and disease in regional lymph node from PET-CT thoracic images. Abnormalities are first detected based on the low-level intensity and Contrast-type features, with a two-level SVM classification. The detected abnormalities are then differentiated into tumors or abnormal lymph nodes with a CRF model, based on the unary level Contextual and spatial features and pairwise-level spatial features. Another CRF model is then employed to relabel the detected tumors as either true tumor or mediastinum by filtering the high-uptake myocardium areas. The detection recall and precision were measured for each stage, and the discriminative power of each feature set was also evaluated. On a clinical dataset of 93 tumor and 65 abnormal lymph nodes from 85 3-D image sets, we found the proposed method showed high detection performance and capability in handling a wide variety of abnormal patterns. We are working on further reducing the false negatives of abnormal lymph nodes, which were produced due to undetected abnormalities or mislabeled as tumors, accounting for the 13.8% less recall from a total recall level. In This paper our current investigation is on improving shape analysis by coupling with spatial priors for better lymph node detection, while avoiding any impact on tumor detection. Here STANFORD MODEL is used. This model is based on mathematical steps which are satisfying existing MSD model. So this Modification on this system gives a higher Efficiency on Medical image processing operations. The idea for the watershed transform comes from topography. A body of water and the surrounding region from which the Water drains into it is called a catchment basin.

REFERENCES

- [1] World Health Organization, “Cancer, fact sheet no. 297,” 2011
[Online]. Available: <http://www.who.int/mediacentre/factsheets/fs297/>
- [2] , S. Edge, D. Byrd, C. Compton, A. Fritz, F. Greene, and A. Trotti, Eds., *AJCC Cancer Staging Handbook*, 7th ed. New York: Springer, 2010.
- [3] W. Wever, S. Stroobants, J. Coolen, and J. Verschakelen, “Integrated PET/CT in the staging of nonsmall cell lung cancer: Technical aspects and clinical integration,” *Eur. Respir. J.*, vol. 33, pp. 201–212, 2009.
- [4] Y. Song, W. Cai, S. Eberl, M. Fulham, and D. Feng, “Discriminative pathological context detection in thoracic images based on multi-level inference,” in *MICCAI 2011, LNCS*, 2011, vol. 6893, pp. 185–192.
- [5] C. Cortes and V. Vapnik, “Support-vector networks,” *Mach. Learn.*, vol. 20, no. 3, pp. 273–297, 1995.
- [6] J. Lafferty, A. McCallum, and F. Pereira, “Conditional random fields: Probabilistic models for segmenting and labeling sequence data,” in *Proc. ICML*, 2001, pp. 282–289.
- [7] Y. Song, W. Cai, S. Eberl, M. Fulham, and D. Feng, “Thoracic image case retrieval with spatial and contextual information,” in *Proc. ISBI*, 2011, pp. 1885–1888.
- [8] I. Jafar, H. Ying, A. Shields, and O. Muzik, “Computerized detection of lung tumors in PET/CT images,” in *Proc. EMBC*, 2006, pp. 2320–2323.
- [9] Y. Cui, B. Zhao, T. Akhurst, J. Yan, and L. Schwartz, “CT-guided automated detection of lung tumors on PET images,” in *SPIE Med. Imag.*, 2008, vol. 6915, p. 69152N.
- [10] C. Ballangan, X. Wang, S. Eberl, M. Fulham, and D. Feng, “Automated lung tumor segmentation for whole body PET volume based on novel downhill region growing,” in *SPIE Med. Imag.*, 2010, vol. 7623, p. 76233O.
- [11] J. Gubbi, A. Kanakatte, T. Kron, D. Binns, B. Srinivasan, N. Mani, and M. Palaniswami, “Automatic tumour volume delineation in respiratory gated PET images,” *J. Med. Imag. Radia. Oncol.*, vol. 55, pp. 65–76, 2011.
- [12] G. Saradhi, G. Gopalakrishnan, A. Roy, R. Mullick, R. Manjeshwar, K. Thielemans, and U. Patil, “A framework for automated tumor detection in

thoracic FDG PET images using texture-based features,” in *Proc.ISBI*, 2009, pp. 97–100.

[13] S. Renisch, R. Opfer, and R. Wiemker, “Towards automatic determination of total tumor burden from PET images,” in *SPIE Med. Imag.*, 2010, vol. 7624, p. 76241T.

[14] Y. Song, W. Cai, S. Eberl, M. Fulham, and D. Feng, “Automatic detection of lung tumor and abnormal regional lymph nodes in PET-CT images,” *J. Nucl. Med.*, vol. 52, p. 211, 2011.

[15] H. Gutte, D. Jakobsson, F. Olofsson, M. Ohlsson, S. Valind, A. Loft, L. Edenbrandt, and A. Kjaer, “Automated interpretation of PET/CT images in patients with lung cancer,” *Nucl. Med. Commun.*, vol. 28, no. 2, pp. 79–84, 2007.

[16] A. Kiraly, L. Zhang, C. Novak, D. Naidich, and L. Guendel, “Novel method and applications for labeling and identifying lymph nodes,” in *SPIE Med. Imag.*, 2007, vol. 6911, p. 691111.

[17] K. Lu, S. Merritt, and W. Higgins, “Extraction and visualization of the central chest lymph-node stations,” in *SPIE Med. Imag.*, 2008, vol. 6915, p. 69151B.

[18] M. Feuerstein, D. Deguchi, T. Kitaska, S. Iwano, K. Imaizumi, Y. Hasegawa, Y. Suenaga, and K. Mori, “Automatic mediastinal lymph node detection in chest CT,” in *SPIE Med. Imag.*, 2009, vol. 7260, p. 72600.

[19] J. Feulner, S. K. Zhou, M. Huber, J. Hornegger, D. Comaniciu, and A. Cavallaro, “Lymph nodes detection in 3-D chest CT using a spatial prior probability,” in *Proc. CVPR*, 2010, pp. 2926–2932.

[20] M. Feuerstein, B. Glocker, T. Kitaska, Y. Nakamura, S. Iwano, and K. Mori, “Mediastinal atlas creation from 3-D chest computed tomography images: Application to automated detection and station mapping of lymph nodes,” *Med. Image Anal.*, vol. 16, no. 1, pp. 63–74, 2011.

[21] T. Kitaska, Y. Tsujimura, Y. Nakamura, K. Mori, Y. Suenaga, M. Ito, and S. Nawano, “Automated extraction of lymph nodes from 3-D abdominal CT images using 3-D minimum directional difference filter,” in *MICCAI 2007, LNCS*, 2007, vol. 4792, pp. 336–343.

[22] A. Bardu, M. Suehling, X. Xu, D. Liu, S. Zhou, and D. Comaniciu, “Automatic detection and segmentation of axillary lymph nodes,” in *MICCAI 2010, LNCS*, 2010, vol. 6361, pp. 28–36.

[23] H. Zaidi and I. E. Naqa, “PET-guided delineation of radiation therapy treatment volumes: A survey of image segmentation techniques,” *Eur. J. Nucl. Med. Mol. Imag.*, vol. 37, no. 11, pp. 2165–2187, 2010.

[24] J. Kuhnigk, V. Dicken, L. Bornemann, A. Bakai, D. Wormanns, S. Krass, and H. Peitgen, “Morphological segmentation and partial volume analysis for volumetry of solid pulmonary lesions in thoracic CT scans,” *IEEE Trans. Med. Imag.*, vol. 25, no. 4, pp. 417–434, Apr. 2006.

[25] M. Kakar and D. R. Olsen, “Automatic segmentation and recognition of lungs and lesions from CT scans of thorax,” *Comput. Med. Imag. Graph.*, vol. 33, no. 1, pp. 72–82, 2009.

[26] Q. Song, M. Chen, J. Bai, M. Sonka, and X. Wu, “Surface-region context in optimal multi-object graph-based segmentation: Robust delineation of pulmonary tumors,” in *IPMI 2011, LNCS*, 2011, vol. 6801, pp. 61–72.

[27] V. Potesil, X. Huang, and X. Zhou, “Automated tumour delineation using joint PET/CT information,” in *SPIE Med. Imag.*, 2007, vol. 6514, p. 65142Y.

[28] H. Gribben, P. Miller, G. Hanna, K. Carson, and A. Hounsell,

“MAP-MRF segmentation of lung tumours in PET/CT images,” in

Proc. ISBI, 2009, pp. 290–293.

[29] J. Wojak, E. Angelini, and I. Bloch, “Joint variational segmentation of CT-PET data for tumoral lesions,” in *Proc. ISBI*, 2010, pp. 217–220.

[30] J. Yan, T. Zhuang, B. Zhao, and L. Schwartz, “Lymph node segmentation from CT images using fast marching method,” *Comput. Med. Imag. Graph.*, vol. 28, no. 1–2, pp. 33–38, 2004.

[31] J. Yan, B. Zhao, L. Wang, A. Zelenetz, and L. Schwartz, “Marker-controlled watershed for lymphoma segmentation in sequential CT images,” *Med. Phys.*, vol. 33, no. 7, pp. 2452–2460, 2006.

[32] D. Maleike, M. Fabel, R. Tetzlaff, H. Tenggekøgligk, T. Heimann, H. Meinzer, and I. Wolf, “Lymph node segmentation on CT images by a shape model guided deformable surface method,” in *SPIE Med. Imag.*, 2008, vol. 6914, p. 69141S.

[33] Y. Song, W. Cai, S. Eberl, M. Fulham, and D. Feng, “A content-based image retrieval framework for multi-modality lung images,” in *Proc. CBMS*, 2010, pp. 285–290.

- [34] A. Vedaldi and S. Soatto, “Quick shift and kernel methods for mode seeking,” in *ECCV 2008, LNCS*, 2008, vol. 5305, pp. 705–718.
- [35] C.-C. Chang and C.-J. Lin, “LIBSVM: A library for support vector machines,” *ACM Trans. Intell. Syst. Technol.* vol. 2, pp. 27:1–27:27, 2011 [Online]. Available: <http://www.csie.ntu.edu.tw/~cjlin/libsvm>
- [36] J. Shotton, J. Winn, C. Rother, and A. Criminisi, “Textonboost: Joint appearance, shape and context modeling for multi-class object recognition and segmentation,” in *ECCV 2006, LNCS*, 2006, vol. 3951, pp.1–15.
- [37] Y. Boykov, O. Veksler, and R. Zabih, “Efficient approximate energy minimization via graph cuts,” *IEEE Trans. Pattern Anal. Mach. Intell.*, vol. 20, no. 12, pp. 1222–1239, Dec. 2001.
- [38] V. Kolmogorov and R. Zabih, “What energy functions can be minimized via graph cuts?,” *IEEE Trans. Pattern Anal. Mach. Intell.*, vol. 26, no. 2, pp. 147–159, Feb. 2004.
- [39] Y. Boykov and V. Kolmogorov, “An experimental comparison of min-cut/max-flow algorithms for energy minimization in vision,” *IEEE Trans. Pattern Anal. Mach. Intell.*, vol. 26, no. 9, pp. 1124–1137, Sep. 2004.
- [40] N. Dalal and B. Triggs, “Histograms of oriented gradients for human detection,” in *Proc. CVPR*, 2005, pp. 886–893.
- [41] M. Everingham, L. Gool, C. Williams, J. Winn, and A. Zisserman, “The pascal visual object classes (VOC) challenge,” *Int. J. Comput. Vis.*, vol 8, no. 2, pp. 303–338, 2010.